Design of tapered polarization splitter based on EC-CHFs by full-vectorial FE-BPM using coordinate transformation

Design of Tapered Polarization Splitter Based on EC-CHFs by Full-Vectorial FE-BPM Using Coordinate Transformation

SHINGO KAWAMURA[1], YASUHIDE TSUJI[1,*], AND ZEJUN ZHANG[2]

[1]*Division of Information and Electronic Engineering, Muroran Institute of Technology, Muroran 050-8585, Japan*
[2]*Department of Electrical, Electronics and Information Engineering, Kanagawa University, Yokohama 221-8686, Japan*
Corresponding author: y-tsuji@mmm.muroran-it.ac.jp

We propose and design a tapered polarization splitter (PS) using the single polarization property of an elliptical-hole core circular-hole holey fiber (EC-CHF). It is reported that a polarization splitting without any crosstalk is enabled using the PS with EC-CHF. In this paper, we show that the mode coupling is enhanced with a tapered PS structure and the fully waveguide separation at the input and output ends can be simultaneously realized. We also propose a full-vectorial finite element beam propagation method using coordinate transformation (CT-VFE-BPM) to efficiently analyze a waveguide whose structure varies along the longitudinal direction. In this approach, computational accuracy and efficiency are greatly improved. © 2020 Optical Society of America

1. INTRODUCTION

In recent years, with the rapid increase in communication traffic, high-speed and large-capacity optical communication systems are desired. In order to respond to this demand, high performance optical fibers and optical devices are widely studied. Photonic crystal fibers (PCFs)[1, 2], consisting of a periodical array of air holes around the core region, also known as holey fibers (HFs), have several unique properties that cannot be obtained by the conventional optical fibers, such as flexible dispersion control, high birefringence, high nonlinearity, endlessly single mode transmission, and so on[3, 4]. Single polarization transmission is also one of these unique natures and several kinds of single-polarization PCFs have been proposed[5–9]. Especially, a holey fiber named elliptical-hole core circular-hole holey fiber (EC-CHF), in which elliptical air holes are introduced in the core region, can easily realize single polarization transmission by breaking the structural symmetry[7–9].

A polarization division multiplexing (PDM) system is one of the methods to enable large-capacity communication, and a polarization splitter (PS) which can separate an arbitrary polarized light into two orthogonal polarizations is a key device for a PDM system. Several PCF based PSs have been proposed so far[10–15]. However, in all of these devices the extinction ratio has to be carefully discussed because the crosstalk component causes undesired behavior in PDM systems. In 2014, Zhang *et al.* [16, 17] proposed a PS using EC-CHFs with a device length of 630 μm, for achieving the polarization separation without any crosstalk.

However, since the fibers are still in a coupled state at the input and output ends for the PS in [16], it is necessary to separate the each fiber at the input and output ends. To overcome this problem, we consider a tapered structure of the PS, it is expected that the mode coupling in the waist region can be enhanced and the fully waveguide separation at the input and output ends can be simultaneously realized. In our previous fundamental study[17], equivalent step index fiber approximation method is used to design a tapered PS with small hole EC-CHFs. However, to enhance the birefringence of EC-CHFs, it is prefer to use large air holes. To analyze large hole EC-CHFs, the equivalent step index fiber approximation is not appropriate and an universality design method with high accuracy should be considered.

The beam propagation method (BPM)[18] is widely used for the analysis of optical waveguide devices whose structure slowly varies along the longitudinal direction. Among several types of BPMs, the finite element BPM (FE-BPM)[19, 20] is an effective one to treat waveguide with a complex cross sectional geometry using curved material boundaries, and then it is often employed for analyzing optical devices based on PCFs. However, when utilizing BPM analysis on a waveguide whose structure varies along the longitudinal direction, there is a problem of accuracy degradation due to the error caused by staircase approximation of the waveguide structure along the propagation direction. Several proposals for BPM analysis based on coordinate transformation have been proposed to overcome this problem[21–23]. Furthermore, in the case of FE-BPM, accumulation of computational errors due to the interpolation of the electromagnetic field
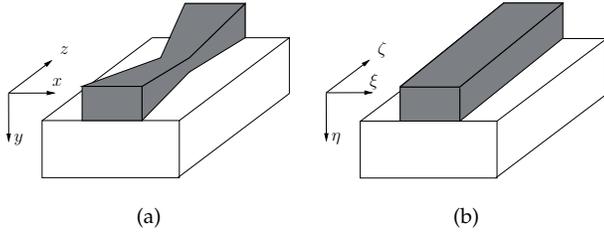
Fig. 1. 3-dimensional tapered optical waveguide. (a)(x, y, z) coordinate system. (b)(ξ, η, ζ) coordinate system.

distribution also becomes a problem.

In this paper, we propose a full-vectorial FE-BPM using co-ordinate transformation (CT-VFE-BPM) to efficiently analyze a waveguide whose structure varies along the longitudinal direction. First, the formulation of the CT-VFE-BPM is described in detail. After that, a tapered PS is designed utilizing our proposed CT-VFE-BPM. We also refer to the wavelength dependence and structure tolerance simultaneously. Finally, the conclusions obtained in this study is stated.

2. FE-BPM USING COORDINATE TRANSFORMATION

A. Coordinate Transformation

When FE-BPM analysis is applied to a waveguide whose structure varies along the longitudinal direction, not only the step approximation of the device along its propagation direction, but also the interpolation of the electromagnetic field at each propagation step accompanied by the finite element update, may degrade the computational accuracy. Transform the original device into a structure with no change along the propagation direction, and then using the FE-BPM may effectively solve the above problems.

We consider a tapered waveguide as shown in Fig. 1(a). A coordinate transformation that transform the tapered waveguide into an equivalent linear waveguide as shown in Fig. 1(b) is given as follows:

$$\begin{cases} x = \xi f(\zeta) \\ y = \eta f(\zeta) \\ z = \zeta \end{cases} . \qquad (1)$$

The partial differential operator for each coordinate variable can be expressed as:

$$\begin{cases} \dfrac{\partial}{\partial x} = \dfrac{1}{f(\zeta)} \dfrac{\partial}{\partial \xi} \\ \dfrac{\partial}{\partial y} = \dfrac{1}{f(\zeta)} \dfrac{\partial}{\partial \eta} \\ \dfrac{\partial}{\partial z} = -\xi \dfrac{f'(\zeta)}{f(\zeta)} \dfrac{\partial}{\partial \xi} - \eta \dfrac{f'(\zeta)}{f(\zeta)} \dfrac{\partial}{\partial \eta} + \dfrac{\partial}{\partial \zeta} \end{cases} , \qquad (2)$$

where $f(\zeta)$ is an approximate function to obtain an equivalent linear waveguide in the (ξ, η, ζ) coordinate system, and is defined in advance for each problem.

B. Formulation of Guided Mode Analysis

We consider a 3-dimensional optical waveguide as shown in Fig. 1(b). The vectorial wave equation is given by the Maxwell's equation as follows:

$$\nabla \times (p \nabla \times \mathbf{\Phi}) - k_0^2 q \mathbf{\Phi} = 0, \qquad (3)$$

where k_0 is the free space wavenumber, ∇ is a coordinate transformed nabla operator, and $\mathbf{\Phi}$, p and q are given by

$$\begin{aligned} p = 1, & \quad q = n^2 \quad \text{for } \mathbf{\Phi} = \mathbf{E}, \\ p = 1/n^2, & \quad q = 1 \quad \text{for } \mathbf{\Phi} = \mathbf{H}. \end{aligned}$$

Then, dividing the $\xi\eta$ cross-section in Fig. 1(b) using the triangular edge/nodal hybrid curvilinear element, and formally assuming light wave through this structure with the propagation constant β, the electromagnetic field vector $\mathbf{\Phi}$ in each element is expressed as follows:

$$\begin{aligned} \mathbf{\Phi}(\xi, \eta, \zeta) &= \phi(\xi, \eta) \exp(-j\beta\zeta) \\ &= \begin{bmatrix} \{U\}^T & \{0\}^T \\ \{V\}^T & \{0\}^T \\ \{0\}^T & j\beta\{N\}^T \end{bmatrix} \begin{bmatrix} \{\phi_t\} \\ \{\phi_\zeta\} \end{bmatrix} \exp(-j\beta\zeta), \end{aligned} \qquad (4)$$

where $\{U\}$, $\{V\}$ are the shape functions of the edge element, $\{N\}$ is the shape function of the nodal element. At this time, the rotation operator of the electromagnetic field vector $\mathbf{\Phi}$ can be expressed as follows:

$$\begin{aligned} \nabla \times \mathbf{\Phi} = \Bigg(& \begin{bmatrix} \xi \dfrac{f'(\zeta)}{f(\zeta)} \dfrac{\partial\{V\}^T}{\partial\xi} + \eta \dfrac{f'(\zeta)}{f(\zeta)} \dfrac{\partial\{V\}^T}{\partial\eta} & \{0\}^T \\ -\xi \dfrac{f'(\zeta)}{f(\zeta)} \dfrac{\partial\{U\}^T}{\partial\xi} - \eta \dfrac{f'(\zeta)}{f(\zeta)} \dfrac{\partial\{U\}^T}{\partial\eta} & \{0\}^T \\ -\dfrac{1}{f(\zeta)} \dfrac{\partial\{U\}^T}{\partial\eta} + \dfrac{1}{f(\zeta)} \dfrac{\partial\{V\}^T}{\partial\xi} & \{0\}^T \end{bmatrix} \\ & -j\beta \begin{bmatrix} -\{V\}^T & \dfrac{1}{f(\zeta)} \dfrac{\partial\{N\}^T}{\partial\eta} \\ \{U\}^T & -\dfrac{1}{f(\zeta)} \dfrac{\partial\{N\}^T}{\partial\xi} \\ \{0\}^T & \{0\}^T \end{bmatrix} \Bigg) \begin{bmatrix} \{\phi_t\} \\ \{\phi_\zeta\} \end{bmatrix} . \end{aligned} \qquad (5)$$

Substituting (4) and (5) into (3) and applying FEM based on Galerkin method, the following equation can be obtained:

$$([K] - j\beta[L] - \beta^2[M])\{\phi\} = \{0\} \qquad (6)$$

where $[K]$, $[L]$ and $[M]$ are finite element matrices and are given by

$$\begin{aligned} [K] &= \begin{bmatrix} [K_{tt}] & [0] \\ [0] & [0] \end{bmatrix}, [L] = \begin{bmatrix} [L_{tt}] & [L_{t\zeta}] \\ [L_{\zeta t}] & [0] \end{bmatrix}, \\ [M] &= \begin{bmatrix} [M_{tt}] & [M_{t\zeta}] \\ [M_{\zeta t}] & [M_{\zeta\zeta}] \end{bmatrix}. \end{aligned}$$

The details of the finite element matrix are described in APPENDIX A.

C. Formulation of Beam Propagation Method

We assume that the light wave propagating in the ζ direction has a propagation constant $jk_0 n_0$. The electromagnetic field $\mathbf{\Phi}$ is divided into the slowly varying envelope amplitude ϕ and the steady propagation term, and is expressed as follows:

$$\mathbf{\Phi}(\xi, \eta, \zeta) = \phi(\xi, \eta, \zeta) \exp(-jk_0 n_0 \zeta) \qquad (7)$$

(a)

(b)
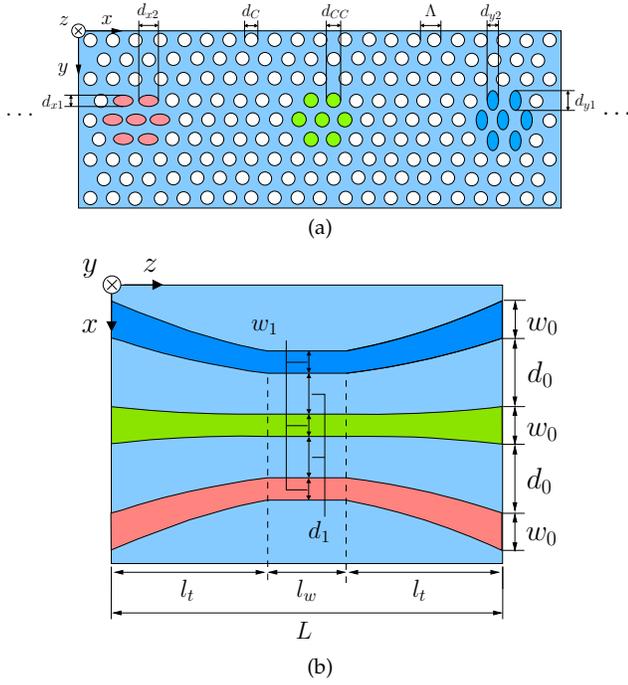
Fig. 2. Structure of the proposed tapered PS. (a) Cross-sectional view, (b) top view.

where n_0 is reference refractive index. Then, replacing $-j\beta$ with $-jk_0n_0 + d/d\zeta$ in (6) and using the Fresnel approximation, the basic equation for FE-BPM is obtained as follows:

$$([L] - j2k_0n_0[M])\frac{d\{\phi\}}{d\zeta}$$
$$+ ([K] - jk_0n_0[M])\{\phi\} = \{0\}. \tag{8}$$

Finally, applying the difference method based on the θ scheme in the ζ direction, the sequential updating equation of FE-BPM is given as:

$$[A]_{i+\frac{1}{2}}\{\phi\}_{i+1} = [B]_{i+\frac{1}{2}}\{\phi\}_i, \tag{9}$$

with

$$[A]_i = ([L]_i - 2jk_0n_0[M]_i)$$
$$+ \theta\Delta\zeta([K]_i - jk_0n_0[L]_i - k_0^2n_0^2[M]_i)$$
$$[B]_i = ([L]_i - 2jk_0n_0[M]_i)$$
$$+ (1-\theta)\Delta\zeta([K]_i - jk_0n_0[L]_i - k_0^2n_0^2[M]_i),$$

where $\Delta\zeta$ represents the step size along the ζ direction, the subscripts i and $i+1$ represent the i-th and $(i+1)$-th propagation step, respectively. Employing this formulation, only once finite element mesh generation at the incident port is required, and the analysis of a waveguide whose structure varies along the longitudinal direction can be performed only by calculating a finite element matrix at each propagation step. The accuracy of the proposed CT-VFE-BPM is briefly discussed in APPENDIX B.

3. DESIGN OF TAPERED PS

Here, a tapered PS based on the large-hole EC-CHF [17] is designed using the CT-VFE-BPM. Figure 2 shows the structure of the tapered PS. A y-polarized EC-CHF (yEC-CHF) and an x-polarized EC-CHF (xEC-CHF) are placed on both sides of

(a)x-polarization.

(b)y-polarization.
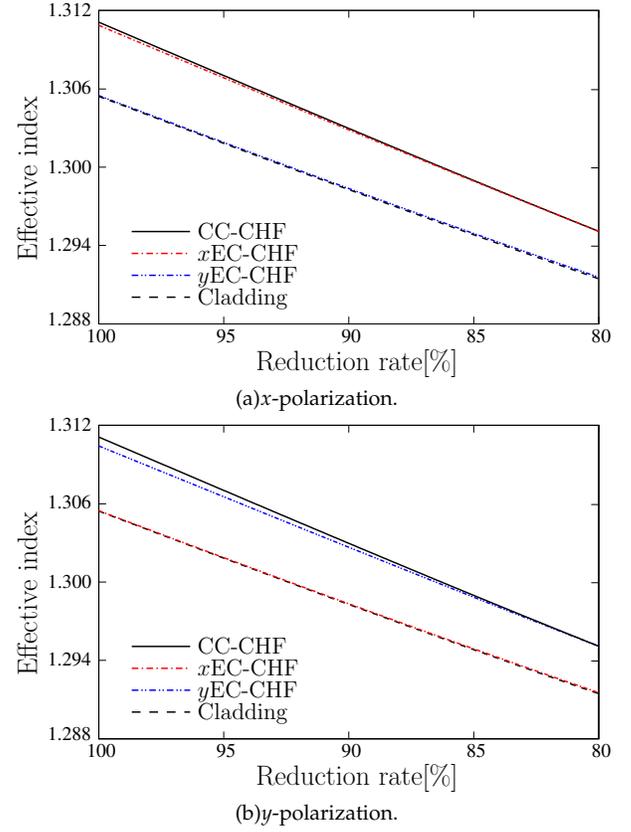
Fig. 3. Waveguide reduction ratio dependence of effective refractive index of each EC-CHFs.

the circular-hole core circular-hole holey fiber (CC-CHF). In our design procedure, the hole sizes for each EC-CHF at the waist region are firstly designed. The hole diameter of yEC-CHF is determined as a reference waveguide, then, the hole diameters of CC-CHF and xEC-CHF are designed respectively to meet the phase matching condition with the yEC-CHF. Next, longitudinal taper structure is used so that the waveguide is sufficiently separated at the input and output ends. The taper and waist lengths are determined by maximizing the light coupling into each single-polarization fiber. Finally, the wavelength dependence and structural tolerance of the designed tapered PS are described in detail.

A. Design of Cross-sectional Structure

Fig. 2 (a) shows the cross-sectional geometry of the tapered PS using large-hole EC-CHFs. Structural parameters are determined based on the values in [17]. The lattice pitch Λ is 1.24 μm, the major axis of the yEC-CHF $d_{y1} = 0.9\Lambda$, the ellipticity $d_{y1}/d_{y2} = 2$, the air hole diameter in the cladding region $d_C = 0.65\Lambda$, the refractive indices of silica and air holes are $n_1 = 1.45$ and $n_2 = 1$, respectively, and the operating wavelength is assumed to be $\lambda = 1.55$ μm. Then, in order to sufficiently separate the waveguide at the input and output ends, the distance between two adjacent cores is selected to be larger than that in [17]. The distance has a trade-off relationship between device length and sufficient waveguide separation. If the distance is increased, the coupling at the input and output ends can be almost eliminated. However, if the distance is too large, the coupling at the waist region will be weakened resulting in a long device length.
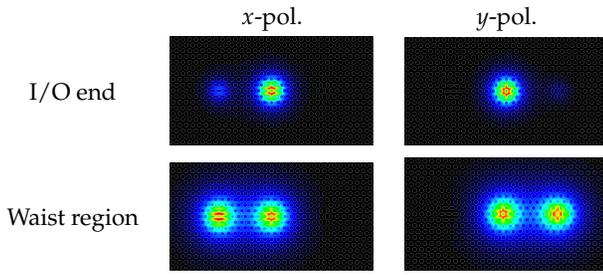
Fig. 4. Fundamental eigenmode field distributions. (Upper row) Input and output ends and (Bottom row) waist region.
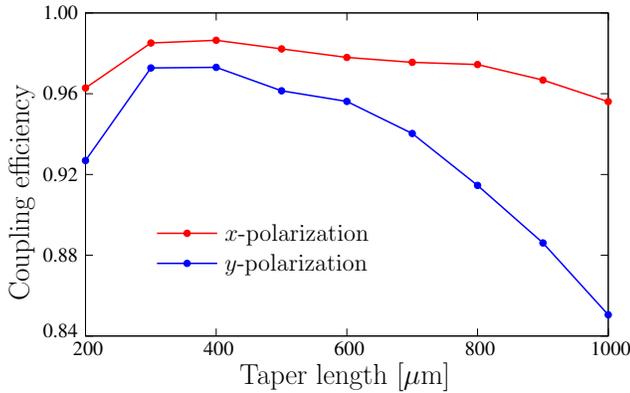
Fig. 5. Taper length dependence of coupling efficiency. The waist length is set to an optimum value.

The number of holes between each adjacent cores was set to three in [17], however, the light coupling at the output end was not negligible because the waveguide separation is not considered in [17]. Therefore, in this paper, the number of air holes between the core is selected to be five to obtain sufficient waveguide separation at the input and output ends. In this paper, the reduction ratio is defined as the ratio of the core diameters at waist region and input/output end. Although a large reduction ratio can shorten the overall device length, it also causes a weak light confinement of the EC-CHF and results a large insertion loss at the taper region. Therefore, the reduction ratio is set to 80% in this paper.

In order to operate this device as a PS, it is necessary to ensure that the three EC-CHFs at the waist region meet the phase matching condition. The hole diameters of CC-CHF and xEC-CHF are determined as $d_{CC} = 0.6099\Lambda$ and $d_{x2} = 0.9146\Lambda$, respectively. Each core of this PS is designed to support only fundamental mode. Figure 3 shows the effective refractive indices of each EC-CHF as a function of reduction ratio. A slight phase mismatch is observed at the input/output end because the air hole diameters in each core is determined considering the phase matching condition at the waist region. Figure 4 shows the fundamental eigenmode field distributions of the coupled system at the input and output ends and the waist region. Although the eigenmodes seems to lies in coupled state, the coupling length estimated from the even and odd modes is sufficiently large compared with that in the waist region.

B. Taper and Waist Lengths

Next, the taper and waist lengths have to be determined. In this paper, the exponential taper shape with taper length of l_t as shown in Fig. 2(b) is employed. The waist length is l_w and the total device length is $L = 2l_t + l_w$. In this case, the coordinate transformation relation between (x, y, z)-coordinate and transformed (ξ, η, ζ)-coordinate is given as follows:

$$f(\zeta) = \begin{cases} \exp\left\{ \left(\dfrac{1}{l_t} \ln \dfrac{w_1}{w_0} \right) \left(\left| \dfrac{L}{2} - \zeta \right| - \dfrac{L}{2} \right) \right\} & \text{in taper} \\ \dfrac{w_1}{w_0} & \text{in waist} \end{cases}.$$

(10)

Figure 5 shows the taper length dependence of the maximum coupling efficiency for the x and y polarization modes. In this calculation, the waist length is set to an optimum value to achieve the maximum power transition at the output end. Since the taper angle is steep with a short taper length, the insertion loss at the taper region becomes large. On the other hand, when the taper length is long, since the influence of the slightly phase mismatched coupling at the tapered region is larger than the phase matched coupling at the waist region, the power transition is diminished.

The taper length with the highest maximum coupling efficiency for x and y polarizations is $l_t = 400$ μm, and the waist length is $l_w = 770$ μm, and the propagation behavior simulated by the CT-VFE-BPM in the PS with these structural parameters is shown in Fig. 6. We can see that the x-polarized wave is coupled only to the xEC-CHF, and the y-polarized wave is coupled only to the yEC-CHF. This results indicates that there is essentially no polarization crosstalk because xEC-CHF and yEC-CHF support only x- or y-polarized wave. The total transmission power of xEC-CHF and yEC-CHF at the output end are 98.7% and 97.5%, respectively, and the insertion loss is only about 2.5%, at wavelength of 1.55 μm. Thus, by designing each structural parameters to an appropriate values, it is possible to obtain a low-loss tapered polarization splitter realizing sufficient waveguide separation at the input and output ends.

In this paper, only the waveguide separation, that is polarization separation, is discussed within this PS. If the output single polarized wave is led to other types of fiber, the excess splice loss may occur. It is reported that the coupling efficiency between a large air hole EC-CHF and standard single mode fiber (SMF) is about 97% when core radius of SMF is optimally selected[24].

C. Characteristics of Designed PS

Figure 7 shows the wavelength dependence of the coupling efficiency of the designed PS. The bandwidth in which the coupling efficiency is greater than 90% is about 100 nm (1505 nm to 1605 nm), in the C-band. Although this bandwidth seems to be narrower than that of PS in [17], this is due to the influence of the tapered region that does not satisfy the phase matching condition. The PS in [17] is not designed considering waveguide separation at input and output ends.

Next, we investigate the structural tolerance of the designed PS. Since elliptical air holes are more difficult to be manufactured than circular air holes, it is necessary to estimate the structural tolerance. Here, the coupling efficiency degradation is investigated when a fabrication error occurs in the hole diameter of x and yEC-CHFs. The coupling efficiencies as a function of the fabrication error are shown in Fig. 8. It can be seen that the insertion loss is increased by relatively small deviation of the air hole size in the core because the phase mismatching between each fiber is increased. In this analysis, we consider that all the hole sizes in the core except for the CC-CHF are deviated, because that is the worst case. In the case of random deviation of the hole size, the
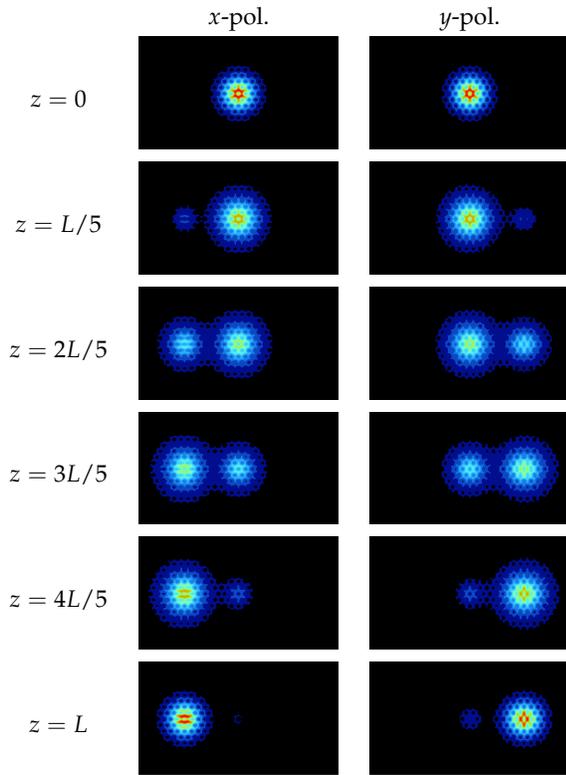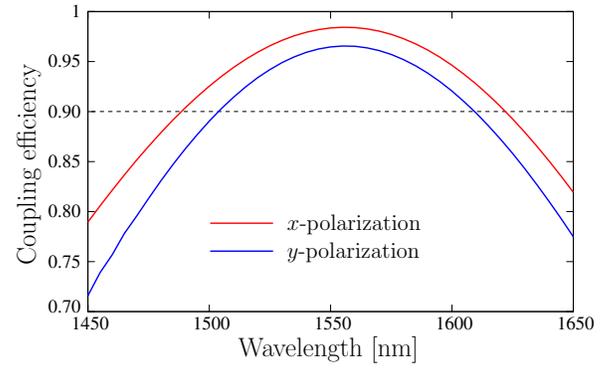
Fig. 6. Propagation behavior in the designed PS.

Fig. 7. Wavelength dependence of the designed PS.

Fig. 8. Structural tolerance of the designed PS.

phase mismatching is mitigated and the fabrication tolerance may be a little bit improved. In any case, the crosstalk component is not coupled to the undesired EC-CHFs. In Fig. 8, we can also see that the maximum coupling efficiency is obtained in the negatively deviated structure compared with the designed one. This is because the propagation constant matching condition is considered only at the waist region, therefore, the propagation constant matching condition is not necessarily satisfied except for the waist region. In the taper region, the structure at waist region is simply expanded and the phase constant has slightly different dependence with the lattice pitch. In addition, propagating directions of both side EC-CHFs are slightly deviated from the z-direction. This may slightly reduce the phase constant of EC-CHFs along the z-direction. If the reduction ratio is further increased and the taper length can be shortened, there is a possibility that a high-performance tapered PS with high structural tolerance can be designed.
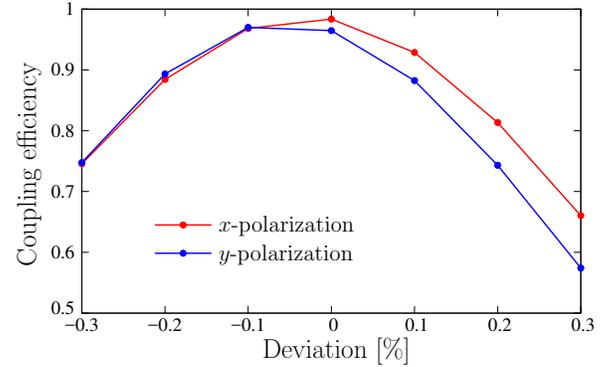
In the above discussion, we consider the major axes of the elliptical air holes are oriented along x- or y-direction. Although crosstalk does not occur in the ideal structure[16], a crosstalk may occur if a fabrication error occurs. In the case that the orientation angle of all the elliptical air holes is deviated from the ideal direction (x- or y-direction), it is considered that a crosstalk occurs almost proportion to $\sin^2 \theta$ when all the elliptical air holes rotate by θ from the ideal direction. The crosstalk is less than -30 dB if θ is less than $1.7°$. However, the crosstalk increases up to about -20 dB if θ is $5°$.

4. CONCLUSION

In this paper, the tapered PS based on the single-polarized EC-CHF is designed considering a practical application of the waveguide separation at input and output end. It was also shown that a device can be efficiently designed using the CT-VFE-BPM. In addition, we investigated the transmission characteristics of the designed PS in detail and indicated that it can operate in wide wavelength band. We do not have any fabrication and measurement environment for PCF in our laboratory. Then, we could not show the experimental results. We think the experimental verification is our next issue. In addition, PS will be designed using a practical PCF with high structural tolerance, and the CT-VFE-BPM will be improved to apply to any longitudinal structural variation.

FUNDING

DISCLOSURES

The authors declare no conflicts of interest.

APPENDIX A: FINITE ELEMENT MATRIX AFTER COORDINATE TRANSFORMATION

The finite element matrix formulated in Section II is described in detail. $[K]$, $[L]$, $[M]$ are given as follows:

$$[K] = \begin{bmatrix} [K_{tt}] & [0] \\ [0] & [0] \end{bmatrix}, [L] = \begin{bmatrix} [L_{tt}] & [L_{t\zeta}] \\ [L_{\zeta t}] & [0] \end{bmatrix},$$

$$[M] = \begin{bmatrix} [M_{tt}] & [M_{t\zeta}] \\ [M_{\zeta t}] & [M_{\zeta\zeta}] \end{bmatrix}.$$

$$[K_{tt}] = \sum_e \iint_e \left[p \left(\left(\xi \frac{f'(\zeta)}{f(\zeta)} \right)^2 (\{U_\xi\}\{U_\xi\}^T + \{V_\xi\}\{V_\xi\}^T) \right. \right.$$
$$+ \left(\eta \frac{f'(\zeta)}{f(\zeta)} \right)^2 (\{U_\eta\}\{U_\eta\}^T + \{V_\eta\}\{V_\eta\}^T)$$
$$+ \xi\eta \left(\frac{f'(\zeta)}{f(\zeta)} \right)^2 (\{U_\xi\}\{U_\eta\}^T + \{U_\eta\}\{U_\xi\}^T$$
$$+ \{V_\xi\}\{V_\eta\}^T + \{V_\eta\}\{V_\xi\}^T)$$
$$\left. + \left(\frac{1}{f(\zeta)} \right)^2 (\{U_\eta\} - \{V_\xi\}^T)(\{U_\eta\} - \{V_\xi\}^T) \right)$$
$$\left. - k_0^2 q(\{U\}\{U\}^T + \{V\}\{V\}^T) \right] d\xi d\eta$$

$$[L_{tt}] = \sum_e \iint_e \left[p \frac{f'(\zeta)}{f(\zeta)} \left(\xi(\{U_\xi\}\{U\}^T - \{U\}\{U_\xi\}^T \right. \right.$$
$$+ \{V_\xi\}\{V\}^T - \{V\}\{V_\xi\}^T)$$
$$+ \left(\eta(\{U_\eta\}\{U\}^T - \{U\}\{U_\eta\}^T \right.$$
$$\left. \left. + \{V_\eta\}\{V\}^T - \{V\}\{V_\eta\}^T) \right) \right] d\xi d\eta$$

$$[L_{t\zeta}] = \sum_e \iint_e \left[-p \frac{f'(\zeta)}{f(\zeta)^2} \left(\xi(\{V_\xi\}\{N_\eta\}^T + \{U_\xi\}\{N_\xi\}^T) \right. \right.$$
$$\left. \left. + \eta(\{V_\eta\}\{N_\eta\}^T + \{U_\eta\}\{N_\xi\}^T) \right) \right] d\xi d\eta$$

$$[L_{\zeta t}] = -[L_{t\zeta}]^T$$

$$[M_{tt}] = \sum_e \iint_e p(\{V\}\{V\}^T + \{U\}\{U\}^T) d\xi d\eta$$

$$[M_{t\zeta}] = \sum_e \iint_e p \frac{1}{f(\zeta)} (\{V\}\{N_\eta\}^T + \{U\}\{N_\xi\}^T) d\xi d\eta$$

$$[M_{\zeta t}] = -[M_{t\zeta}]^T$$

$$[M_{\zeta\zeta}] = \sum_e \iint_e \left[p \left(\frac{1}{f(\zeta)} \right)^2 (\{N_\eta\}\{N_\eta\}^T + \{N_\xi\}\{N_\xi\}^T) \right.$$
$$\left. - k_0^2 q\{N\}\{N\}^T \right] d\xi d\eta$$

APPENDIX B: COMPARISON OF VFE-BPM AND CT-VFE-BPM

In order to show the effectiveness of CT-VFE-BPM, we compare the results of CT-VFE-BPM and the conventional VFE-BPM[25]. In this discussion, we employ the directional coupler consists of equivalent step index (SI) fibers of EC-CHFs. The designed PS with EC-CHFs is difficult to be solved by conventional VFE-BPM because of the accumulation of interpolation errors caused by finite element mesh update process at each propagation step which is required when the cross-sectional geometry is changed in longitudinally varying waveguides. This accumulated error is possible to increase when propagation step size Δz is reduced to
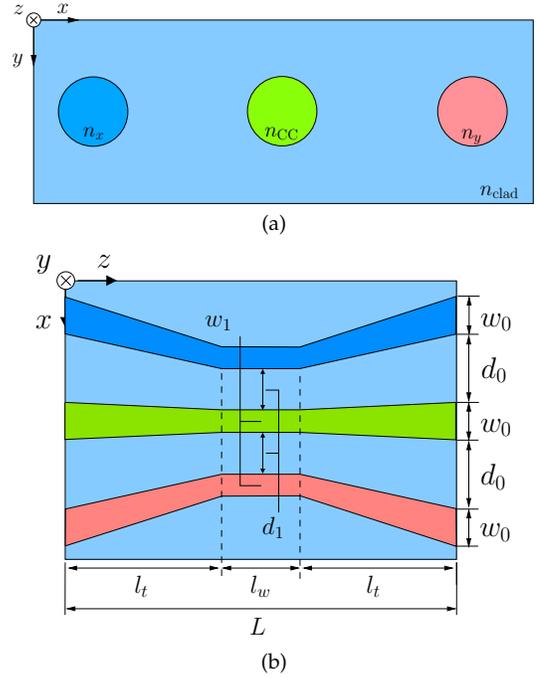
**Fig. 9.** Structure of the directional coupler with equivalent SI fibers. (a) Cross-sectional view, (b) top view.

improve a computational accuracy along the z-direction because the number of mesh update process increases. So, we employ simpler numerical simulation model in this discussion.

We consider a tapered directional coupler with equivalent SI fibers as shown in Fig. 9. Here, we assume the taper shape is linear in order to simplify the problem for the conventional VFE-BPM analysis. The coordinate transformation relation between (x, y, z)-coordinate and transformed (ξ, η, ζ)-coordinate is given as follows:

$$f(\zeta) = \begin{cases} \frac{2(w_0 - w_1)}{w_0 L} \left(\left| \frac{L}{2} - \zeta \right| - \frac{L}{2} \right) + 1 & \text{in taper} \\ \frac{w_1}{w_0} & \text{in waist} \end{cases}. \quad \textbf{(11)}$$

The structural parameters are set to be $l_t = 400 \ \mu m$, $l_w = 810 \ \mu m$, $w_0 = 3.72 \ \mu m$, and $d_0 = 6.2 \ \mu m$, the refractive indices are set to be $n_{CC} = n_y = 1.3253$, $n_x = 1.2955$, $n_{clad} = 1.3059$, and the reduction ratio is set to be 80%. Then, the fundamental E^y mode with a wavelength $\lambda = 1.55 \ \mu m$ is launched into the center SI fiber.

Figure 10 shows the convergence behavior of the calculated coupling efficiency with respect to a degree of freedom (DOF) in FEM used for discretizing transverse direction when $\Delta z = 5 \ \mu m$. The convergence behavior for the longitudinal discretization is also shown by red line for CT-VFE-BPM with DOF of about 2.0×10^5. Although the result by the conventional VFE-BPM does not sufficiently converged, we can see that the results by VFE-BPM is approaching to that by CT-VFE-BPM. In addition, it has been reported that power is not rigorously conserved in the conventional BPM analysis when waveguide structure varies in the longitudinal direction [26]. There is also a possibility that the accuracy is degraded due to the accumulation of interpolation errors at each propagation steps. To obtain sufficient convergence of the solution in VFE-BPM analysis, considerable unknown variables are required. On the other hand, we can see
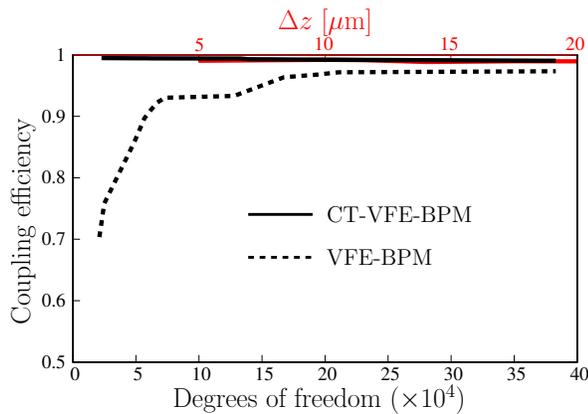
Fig. 10. Calculated coupling efficiency of PS with equivalent SI fibers as a function of degree of freedom in FEM.

that CT-VFE-BPM can obtain more accurate result with fewer unknown variables. Numerical results are in good convergence using this degree of discretization both in transverse and longitudinal direction. The validity of the numerical simulation with coordinate transformation is also demonstrated in the case of scalar approximated analysis in [27].

REFERENCES

1. J. C. Knight, T. A. Birks, P. S. J. Russell, and D. M. Atkin, "All-silica single-mode optical fiber with photonic crystal cladding," Opt. Lett. **21**, 1547–1549 (1996).

2. P. S. J. Russell, "Photonic-crystal fibers," J. Light. Technol. **24**, 4729–4749 (2006).

3. T. A. Birks, J. C. Knight, and P. S. J. Russell, "Endlessly single-mode photonic crystal fiber," Opt. Lett. **22**, 961–963 (1997).

4. J. Broeng, D. Mogilevstev, E. Barkou, and A. Bjarklev, "Photonic crystal fibers: A new class of optical waveguides," Opt. Fiber Lett. **5**, 305–330 (1999).

5. K. Suzuki, H. Kubota, and S. kawanishi, "Optical properties of a low-loss polarization-maintaining photonic crystal fiber," Opt. Express **9**, 676–680 (2001).

6. J. Ju, W. Jin, and M. S. Demokean, "Design of single-polarization single-mode photonic crystal fiber at 1.30 and 1.55 μm," J. Light. Technol. **24**, 825–830 (2006).

7. K. Saitoh and M. Koshiba, "Single-polarization single-mode photonic crystal fibers," IEEE Photonics Technol. Lett. **30**, 1384–1386 (2003).

8. M. Eguchi and Y. Tsuji, "Single-mode single-polarization holey fiber using anisotropic fundamental space-filling mode," Opt. Lett. **32**, 2112–2114 (2007).

9. M. Eguchi and Y. Tsuji, "Design of single-polarization elliptical-hole core circular-hole holey fibers with zero dispersion at 1.55 μm," J. Opt. Soc. Am. B **25**, 1690–1701 (2008).

10. L. Zhang and C. Yang, "Polarization splitter based on photonic crystal fibers," Opt. Express **11**, 1015–1020 (2003).

11. L. Zhang and C. Yang, "A novel polarization splitter based on the photonic crystal fiber with nonidentical dual cores," IEEE Photonics Technol. Lett. **16**, 1670–1672 (2004).

12. K. Saitoh, Y. Sato, and M. Koshiba, "Polarization splitter in three-core photonic crystal fibers," Opt. Express **12**, 3940–3946 (2004).

13. L. Rosa, F. Poli, M. Foroni, A. Cucinotta, and S. Selleri, "Polarization splitter based on a square-lattice photonic-crystal fiber," Opt. Lett. **31**, 441–443 (2006).

14. M. Chen, B. Sun, Y. Zhang, and X. Fu, "Design of broadband polarization splitter based on partial coupling in square-lattice photonic-crystal fiber," Applyed Opt. **49**, 3042–3048 (2010).

15. H. Jiang, E. Wang, J. Zhang, L. Hu, Q. Mao, Q. Li, and K. Xie, "Polar-

ization splitter based on dual-core photonic crystal fiber," Opt. Express **22**, 30461–30466 (2014).

16. Z. Zhang, Y. Tsuji, and M. Eguchi, "Design of polarization splitter with single-polarized elliptical-hole core circular-hole holey fibers," IEEE Photonics Technol. Lett. **26**, 541–543 (2014).

17. Z. Zhang, Y. Tsuji, and M. Eguchi, "Study on crosstalk-free polarization splitter with elliptical-hole core circular-hole holey fibers," J. Light. Technol. **32**, 3956–3962 (2014).

18. M. D. Feit and J. A. Fleck, "Light propagation in graded-index optical fibers," Applyed Opt. **17**, 3990–3998 (1978).

19. Y. Tsuji and M. Koshiba, "A finite element beam propagation method for strongly guiding and longitudinally varying optical waveguides," J. Light. Technol. **14**, 217–222 (1996).

20. Y. Tsuji, M. Koshiba, and T. Shiraishi, "Finite element beam propagation method for three-dimensional optical waveguide structures," J. Light. Technol. **15**, 1728–1734 (1997).

21. S. Helfert and R. Pregla, "New developments of a beam propagation algorithm based on the method of lines," Opt. Quantum Electron. **27**, 943–950 (1995).

22. S. Sujecki, P. Sewell, T. M. Benson, and P. C. Kendall, "Novel beam propagation algorithms for tapered optical structures," J. Light. Technol. **17**, 2379–2388 (1999).

23. D. Djurdjević, "Accurate modelling of modern photonic devices with complex geometries in transverse plane and longitudinal direction," Sci. Tech. Rev. **LIX**, 30–38 (2009).

24. M. Eguchi and Y. Tsuji, "Influence of reflected radiation waves caused by large mode field and large refractive index mismatches on splice loss evaluation between elliptical-hole lattice core holey fibers and conventional fibers," J. Opt. Soc. Am. B **30**, 410–420 (2013).

25. Y. Tsuji and M. Koshiba, "Adaptive mesh generation for full-vectorial guided-mode and beam propagation solutions," IEEE J. Sel. Top. Quantum Electron. **6**, 163–169 (2000).

26. J. Yamauchi, Y. Nito, and H. Nakano, "A modified semivectorial bpm retaining the effects of the longitudinal field component and its application to the design of a spot-size converter," J. Light. Technol. **27**, 2470–2476 (2009).

27. S. Kawamura, Y. Tsuji, and Z. Zhang, "A study on design of tapered polarization splitter using beam propagation method based on coordinate transformation," IEICE Transactions (Japanese Ed.) **J102-C**, 124–130 (2019).